Edinburgh Research Explorer

Influence of EBR on the structural resistance of RC slabs under quasi-static and blast loading: Experimental testing and numerical analysis

Influence of EBR on the structural resistance of RC slabs under quasi-static and blast loading: experimental testing and numerical analysis

R. Mourão[a,b], A. Caçoilo[a,b], F. Teixeira-Dias[a], A. Maazoun[b,c], T. Stratford[a], D. Lecompte[b]

[a]*Institute for Infrastructure and Environment, School of Engineering, The University of Edinburgh, Edinburgh EH9 3JL, UK*
[b]*Civil and Materials Engineering Department, Royal Military Academy, 1000 Brussels, Belgium*
[c]*Magnel Laboratory for Concrete Research, Ghent University, 9052 Gent, Belgium*

Abstract

Flexural strengthening of reinforced concrete (RC) structures with externally bonded reinforcement (EBR) using carbon fibre-reinforced polymers (CFRP) has in recent years received increased interest from specialists, particularly when dealing with protective structures against terrorist or accidental blast loading. Although a significant number of studies have been conducted on the failure modes of the bonded interface for quasi-static conditions, there is still limited published research on the effects of blast loading. In this paper, RC slabs externally strengthened with CFRP are tested in three-point bending as well as subjected to blast loading. The behaviour of the tested specimens under both loading regimes is evaluated with special focus on the mechanisms that lead to the disruption of the CFRP. It was found that the debonding of the CFRP was caused, in both cases, by the fracture and separation of a thin layer of concrete in the near vicinity of the bonded interface. However, the mechanisms that lead to this failure differ. A numerical model was developed and simulations performed using the finite element (FE) code LS-DYNA to investigate the validity of commonly used simplifications on the modelling of the interface in both cases. It was found that although the modelling technique used to represent the disruption of CFRP under quasi-static conditions provide accurate results, it does not return accurate predictions of the debonding of CFRP under blast loading.

Keywords: Blast loading, reinforced concrete, fibre-reinforced polymer, externally bonded reinforcement, stress wave, finite element modelling

1. Introduction

Events such as accidental explosions, terrorist attacks and detonations in civil or military scenarios, render the research and development in impact resistance and blast mitigation of engineering structures imperative. The need to protect people and infrastructures from high intensity dynamic loading such as blast and shock waves, has been stimulating the interest on the development of new, adaptive and more intelligent approaches to the protection of structures and development of armour systems. Reinforced concrete (RC) is extensively used in civil and military infrastructures, including buildings. During their serving life, buildings might be exposed to the threat scenarios

described above, where the structure is subjected to a load much greater than the design load in a very short period of time. This can result in severe damage to the RC structure, which motivates the study of efficient ways to upgrade such buildings aiming to increase their load bearing capacity.

One method that has attracted the attention of researchers in recent years is the strengthening of RC structures with fibre-reinforced polymers (FRP), due to their high strength-to-weight ratios, corrosion resistance and ease of handling and application. The use of FRP as a retrofit material is a popular technique as it can be installed post-construction without forfeiting usable space and requiring long construction time. Although the behaviour of structures retrofitted by means of this technique has been extensively studied under quasi-static loading and it is now well known, this is not the case when dealing with dynamic impulsive loading, such as blast waves.

Some researchers have reported on the experimental testing of RC structures with externally bonded reinforcement (EBR) subjected to blast loads [1, 2, 3, 4]. These studies, however, describe the efficiency of FRP composites for blast protection mainly in a qualitative way. Razaqpur *et al.* [5] investigated the blast performance of RC panels retrofitted with a cross-shaped 500 mm wide glass fibre-reinforced Polymers (GFRP) strip on both sides of the structure. Both retrofitted and control panels were tested under a blast load generated by the detonation of 22.4 kg of ammonium-nitrate-fuel-oil (ANFO) at a stand-off distance of 3.1 m. The authors concluded that the GFRP retrofitted panel performed significantly better than the control panel in resisting the blast load. The post-blast static strength of the retrofitted panel was 75% higher than that of the un-retrofitted panel. In 2014, Orton *et al.* [3] conducted an experimental program where CFRP was used to strengthen RC beams exposed to close-in detonations. The specimens were tested at scaled distances of 0.4 and 0.6 m/kg$^{1/3}$. Overall, the authors concluded that the use of CFRP improves the blast resistance of RC slabs. Additionally, for the larger scaled distance, the CFRP successfully prevented flying debris and reduced the overall deflections of the slab when compared to control specimens. For the closer scaled distance, the high shock blast pressures shattered the concrete through the thickness of the slab specimen and tore through the back-face CFRP. However, the overall deflection was reduced by approximately 75% relative to the control specimen. More recently, Maazoun *et al.* [4] developed an experimental setup using an explosive driven shock tube (EDST) to load a series of five one-way slabs externally reinforced with bonded CFRP strips with a planar blast wave generated by the detonation of 40 g of C4. One of the slabs is used as a control specimen and the remaining slabs were strengthened with different number of strips. The results indicate that using CFRP as EBR significantly increases the flexural capacity and stiffness of RC slabs under blast loads, with a reduction of up to 47% in the maximum inbound deflection, when four strips of CFRP are used. Here, however, the authors recorded an increase in the rebound deflection of approximately 21%. When retrofitted at both sides with two strips, a decrease in the inbound and rebound deflection of 32 and 21% is observed, respectively, when compared to the control specimen.

2

An increase in the number of cracks with the increase of the number of CFRP strips was also observed, albeit with narrower openings.

Numerical modelling is an efficient tool to study the behaviour of these structures and has been used by a considerable number of authors to characterise the behaviour of RC structures strengthened with FRP under blast loading. Although a considerable amount of numerical work is available in the literature on the use of FRP to enhance the blast resistance of reinforced concrete columns [6, 7, 8, 9, 10], the use of numerical models to simulate slabs and slabs is still limited, mostly due to the lack of characterisation of the concrete-to-FRP interface and its failure during bending deformations.

Lin *et al.* [11] developed a finite element model of an RC panel strengthened with FRP loaded by the detonation of explosive charges. They studied the influence of FRP thickness, the retrofitted surface, stand-off distance, and charge mass on the overall behaviour of the structural element. Their model included the effects of high strain rate on concrete and steel strength. They reported a high sensitivity to the charge mass and stand-off distance, as well as a decrease of maximum and residual deflection of the RC panel for increasing FRP thicknesses. Mutalib *et al.* [12] performed a numerical study in LS-DYNA where a FE model of a FRP-strengthened RC wall with different configurations of anchorage systems was used to simulate the behaviour of the structure under blast loading. It was found that FRP strengthening effectively increases the RC wall blast loading resistance capacity. It was also found that the bond strength plays a significant role in maintaining the composite action between the FRP and the concrete, where the use of anchorage systems to prevent delamination of the FRP can be used as a solution, albeit leading to the rupture of the bonded material due to a concentration of stresses.

In a more recent study, Pezzola *et al.* [13] developed a finite element model of an RC beam retrofitted with FRP. The model was detailed with special attention to the concrete-to-FRP interface, where a tiebreak contact was used to simulate the interfacial behaviour of the epoxy bond. This type of contact, as reported by the author, was calibrated based on one experimental test. The calibrated model was then used to successfully predict the behaviour of a second specimen, with little variation when compared to experimental results. In 2019, Maazoun *et al.* [14] presented a numerical model to predict the behaviour of hollow-core RC slabs with CFRP EBR subjected to close-range explosions. In their model, different concrete material models coupled with the use of a tiebreak contact were implemented to describe debonding of the CFRP. However, only the model where an additional erosion criterion was used was able to correctly predict the local debonding observed in the experimental results. Nevertheless, both material models successfully predicted maximum deflections and crack distributions.

Based on the studies presented above, it becomes clear that a fundamental understanding of the behaviour of externally bonded FRP on reinforced concrete under extreme loading is still lacking in the literature, specially con-

cerning the failure of the FRP-concrete interface. This paper sets a thorough experimental comparison of the bearing capacity of retrofitted specimens under quasi-static and blast loading, aiming to determine if the load-deformation characteristics of quasi-static loaded slab can be used when establishing a dynamic analysis of the structural element, as typically performed when analysing typical reinforced concrete elements. Additionally, a finite element model for each experimental setup is developed and the validity of several modelling assumptions regarding the different loading regimes are discussed for both regimes.

2. Experimental analysis

A series of quasi-static and blast tests were conducted to investigate the influence of bonded CFRP on the flexural capacity of RC slabs under both loading regimes.

2.1. Test specimens

Test specimens consist of five $2.2 \times 0.3 \times 0.06$ [m^3] one-way RC slabs; four of these were tested quasi-statically (QS-1, QS-2, QS-R1, QS-R2) and one under blast loading (B1). The slabs were designed to ensure pure flexural behaviour and to comply with the available resources in the testing facility. All test specimens were reinforced with six 6 mm diameter rebars along the longitudinal direction, and 17 equally spaced rods along the transverse direction, to ensure a uniform 40 mm spacing between the longitudinal reinforcement. Steel rebars were positioned is such a way as to ensure a 20 mm uniform concrete clear cover, as shown in Figure 1(a). The slabs were cast in a custom-made wooden mould, compacted and then cured for 28 days in a curing chamber with 100% relative humidity. Three slabs were then externally reinforced with two CFRP strips applied on the concrete surface with an epoxy resin adhesive. The strips are $1,920$ mm long with a cross section of 15×2.5 [mm^2]. They were applied longitudinal wise with a 140 mm gap between them, each one keeping a 65 mm spacing to the lateral edge of the slab. Acetone was used to remove fine dust particles and oily substances on the strips, ensuring a good bonding surface. A uniform epoxy thickness was ensured by using a rubber dispenser. Figures 1(b) and (c) show the position of the steel reinforcement before concrete pouring and a top view of the slab during the bonding process of the second CFRP, respectively.

2.2. Material properties

Concrete was prepared with cement, gravel with a maximum aggregate size of 17 mm, sand, water and super-plasticisers. The mix proportion of the constituents and quantities for each slab are summarised in Table 1. A set of quasi-static 150 mm cube compression tests was conducted to assess the concrete compression strength, f_c. The average 28-day compressive strength was found to be 50.1 MPa. Steel rods of grade 500 with a diameter of 6 mm
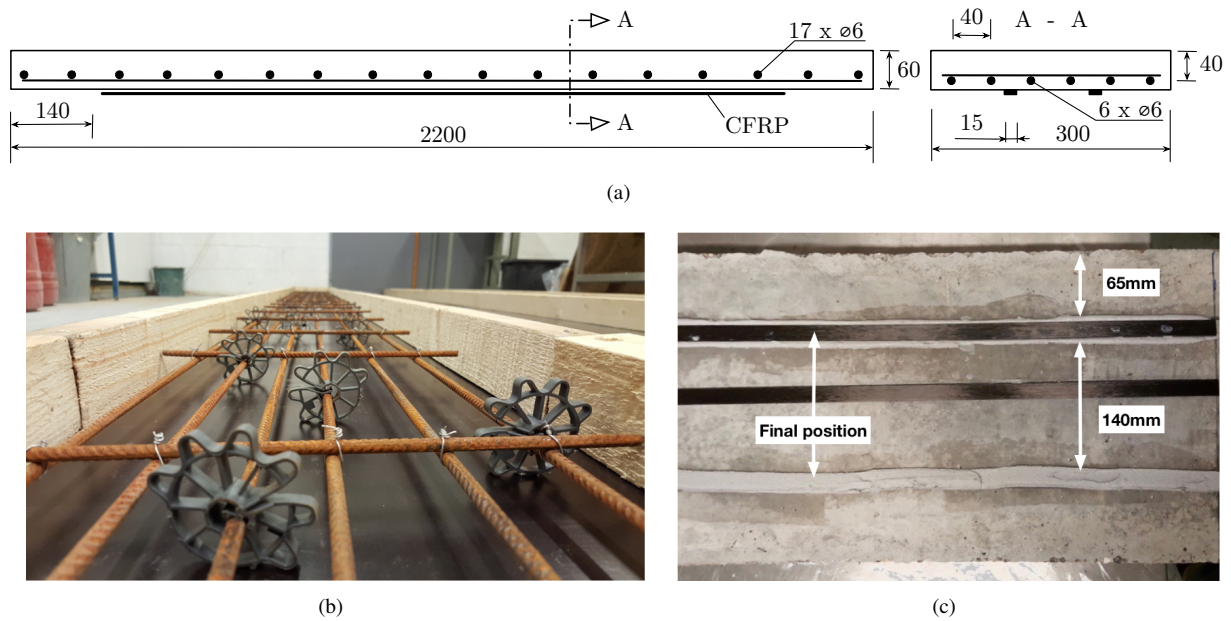
4

Figure 1: (a) Dimensions and reinforcement details of the tested slabs, (b) positioning of the steel reinforcement before concrete pouring and (c) top view of the slab showing the bonding process of the second CFRP strip.

were used as reinforcement. The average yield and ultimate stresses, calculated from 5 trials, were found to be 528.2 and 595.7 MPa, respectively.

Table 1: Mix proportions of concrete.

Component	Sand	Cement	Coarse aggregate	Fine aggregate	Water	Superplasticisers
Mass [kg]	37.5	18.8	17.5	37.5	7.5	0.0375

Strengthening was achieved with pre-fabricated uniaxial CFRP Sika CarboDur S1.525 strips with 15 mm width and 2.5 mm thickness. The epoxy system SikaDur-30 with A and B cold curing agents (resin and hardener, respectively) was used to bond the CFRP strips to concrete. Both epoxy components were mixed in a 3:1 weight ratio of epoxy-to-curing agent, using a low-speed mechanical mixer. The mechanical properties of the CFRP and epoxy, provided by the manufacturer, are listed in Table 2.

2.3. Quasi-static testing

The quasi-static flexural capacity of the specimens was evaluated with horizontal three-point bending tests with displacement control on two control specimens and two externally reinforced with CFRP. A schematic overview of the test setup is shown in Figure 2. Specimens were tested in a simply-supported configuration, allowing the slab to rotate (bend) freely. The distance between supports was 2 m and a single-point displacement was applied on the

5

Table 2: Mechanical properties of the CFRP strips and epoxy system.

Property	Units	SikaDur-30	Sika CarboDur S1.525
Density	kg/m^3	$1,650$	$1,600$
Elastic modulus	GPa	9.6	165
Tensile strength	MPa	24-27	3100
Compression strength	MPa	70-80	–
Shear strength	MPa	14-17	–
Elongation at failure	%	–	1.7

concrete surface with a 10 mm thick 150×30 [mm^2] metal plate as an interface between the slab and the loading device.
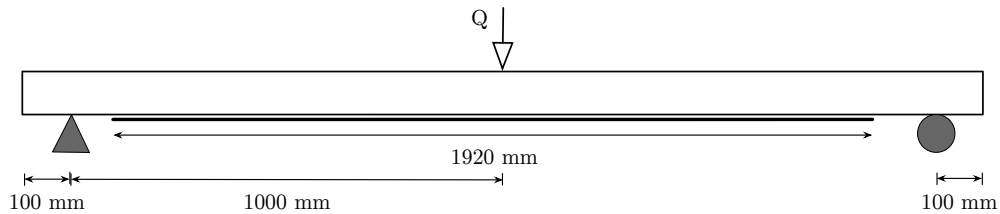

Figure 2: Schematics of the quasi-static test setup.

Figure 3 shows the typical behaviour of the slabs during testing. As the loading was applied in a controlled displacement manner, there is no visual difference between the control and the FRP-strengthened specimens, apart from the disruption of FRP at a certain deflection. A plastic hinge at mid-span with concrete crushing in the outer compression fibre was observed in all specimens.

Figure 4 shows a comparison between the load-deflection data recorded for all the specimens. It can be seen that both control specimens (QS-1 and QS-2) exhibited linear behaviour prior to cracking, which occurred at approximately 1.5 kN, followed by the formation of cracks and increase in deflection. At this stage, two major cracks started to become visible close to the centre of the control specimen. When the load reached 6.9 kN, the steel reinforcement in the control specimen started to yield and the load plateaus while the deflection increased. The compression zone of the slab started to crush when it reached 59 mm of mid-span displacement, at a load of 6.9 kN. Both control specimens developed very similar resistance profiles over displacement.

Considering the addition of CFRP (specimens QS-R1 and QS-R2), although the contribution of the CFRP is effective since the early stages of loading, due to the small thickness of the tested specimens, the increase in stiffness provided by the CFRP was even more noticeable after the appearance of the first crack. The strengthened slabs remained in the elastic-plastic domain up to a load of 13.9 kN and 14.7 kN, where a simultaneous and sudden rip-off of the two CFRP strips was observed. The steel started to yield before the loss of composite action between the CFRP
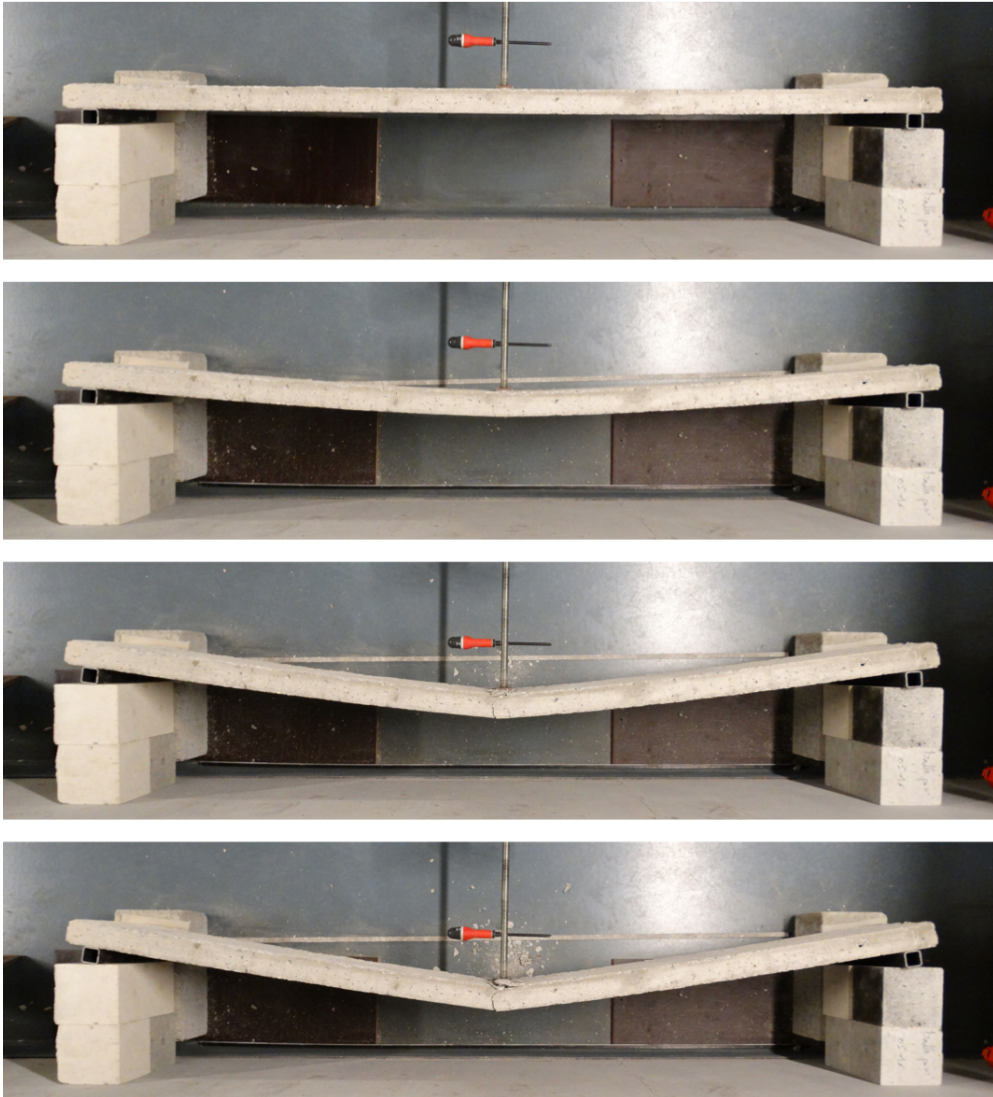
6

Figure 3: Typical behaviour of the slabs during the quasi-static testing.

and the concrete (i.e. debonding) takes place. Debonding is characterised by the detachment of a thin layer of concrete from the slab, as shown in Figure 5. This is one of the main failure mechanisms of the bonded interface due to the high strength characteristics of the adhesive used and is in accordance with the observations of Zheng *et al.* [15]. Since debonding happens in a sudden manner, it is impossible to determine where exactly it initiated.

The debonding of the CFRP was followed by a drop on the load and formation of a plastic hinge in both strengthened specimens. For specimen QS-R1, the load kept somehow constant at approximately 7.2 kN until the failure of the slab, by concrete crushing. Interestingly, the post-debonding behaviour of the slab was found to be similar to the behaviour of control specimens. In general, although the slab strengthened with two strips of CFRP did not show a
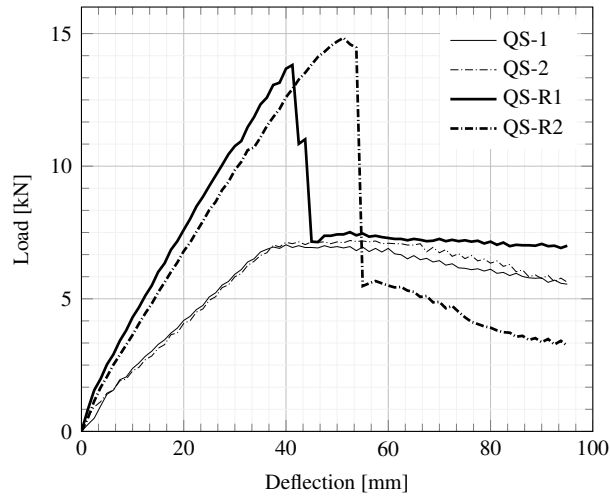
7

Figure 4: Load-deflection history of control and externally reinforced specimens tested in a quasi-static loading regime.

significant increase in the ultimate load when compared to the control slab, the maximum displacement before failure, however, increased by 18% and the maximum load carrying capacity by 115%.

Although specimen QS-R2 exhibited a similar stiffness during the cracking phase, it was able to support a higher peak load before debonding, when comparing to specimen QS-R1. This is certainly caused by the fact that reinforcing strips were manually bonded, being subjected to manufacturing uncertainties. Its residual capacity after the detachment of the EBR was found to be slightly lower than that of the control specimen, for similar displacements, contrarily to specimen QS-R1. Due to the slenderness of the structure, which may lead to damage accumulation during its manipulation, and the high displacement levels achieved, its is not possible to argue about the reason for such observation.

2.4. Blast testing

The blast test was conducted using the experimental setup shown in Figure 6. Specimen B1 was tested in a simply-supported configuration, with an effective span of 2 m, and blast loaded on the face without CFRP. Steel tubes were fixed to the ground and used as supports, with rubber pads placed between the supports and the specimen to ensure uniform support and prevent localised damage. An explosive driven shock tube (EDST) was used to achieve higher pressure and impulses than a free-field air blast loading. This also contributes to higher quality measurements due to the absence of smoke and attenuated flare. A detailed description of the working principle of the EDST can be found in the work of Ousji *et al.* [16]. The EDST is a thin-walled steel square section tube with an edge of 300 mm, 5 mm thick and 1.5 m long. The blast load was generated by the detonation of 50 g of C4, positioned 0.3 m from the entrance of the tube. The charge was suspended inside the tube by an adjustable stand.
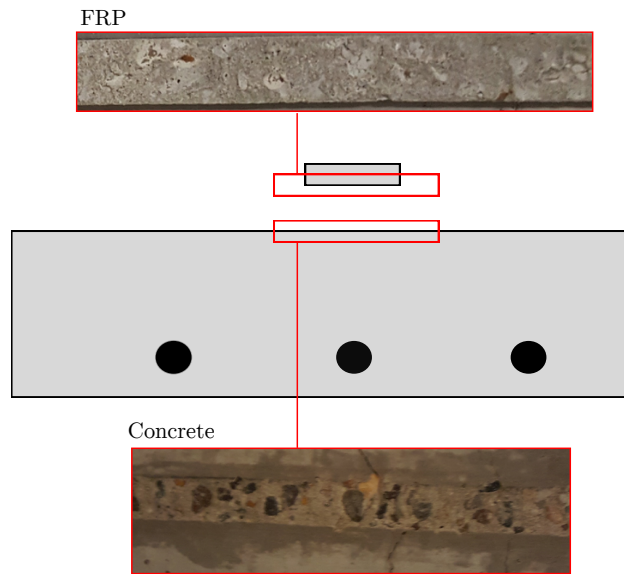
8

Figure 5: CFRP-concrete interface after debonding, with a thin layer of concrete attached to the CFRP strip.
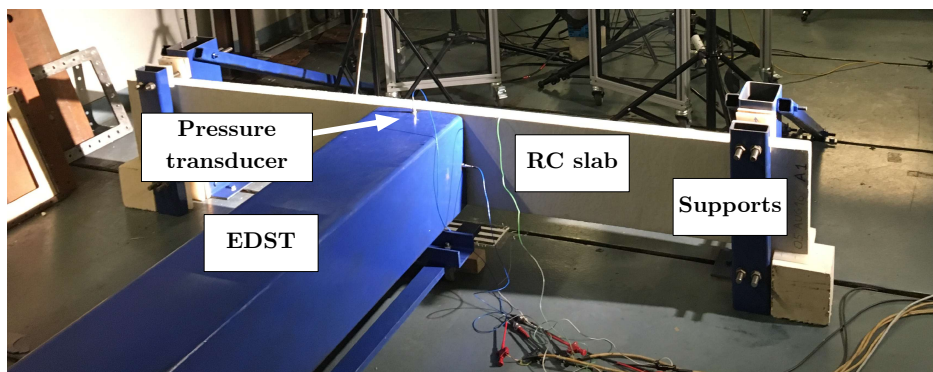

Figure 6: Experimental setup for blast testing.

The overall response of the tested specimen was captured with a Photron SA5 high-speed camera, calibrated to record images at 10k frames per second. To measure the strain in the steel and CFRP, three 10 mm 120 Ω resistance strain gauges were used. Two additional strain gauges were bonded to the tensile face of the reinforcing steel before casting the concrete specimens, at a distance of 0.1 m from the centre of the slab, in both directions. One additional strain gauge was installed on the externally bonded longitudinal CFRP at 0.1 m from the centre (mid-span) of the slab. The mid-span deflection-time history was recorded using a linear variable differential transformer (LVDT) at the concrete surface, with a sampling rate of 4.8 MHz. A pressure transducer was used to measure the incident pressure at 20 mm from the end of the tube and also to serve as a trigger to start the measurements.

Preliminary tests were conducted on the use of the explosive driven shock tube against a thick steel plate. Reflected pressure histories at the end of the shock tube were recorded to describe the pressure distribution on the slab. Three pressure transducers were fixed to the plate in different locations and the resulting pressure profiles and cumulative specific impulse are shown in Figure 7(a) and (b), respectively. The negative phase of the blast wave is almost non-existant and can thus be neglected.

A good agreement between the peak overpressure in all sensors was observed. Although the calculated cumulative specific impulses are similar for sensor 2 and 3, sensor 1 registered slightly higher values from 0.4 ms onwards. This can be explained by the minor pressure peaks visible in the pressure profiles, which may be caused by unexpected vibrations of the sensor. The average maximum recorded overpressure and specific impulse was 7.5 MPa and 1770 Pa.s, respectively.
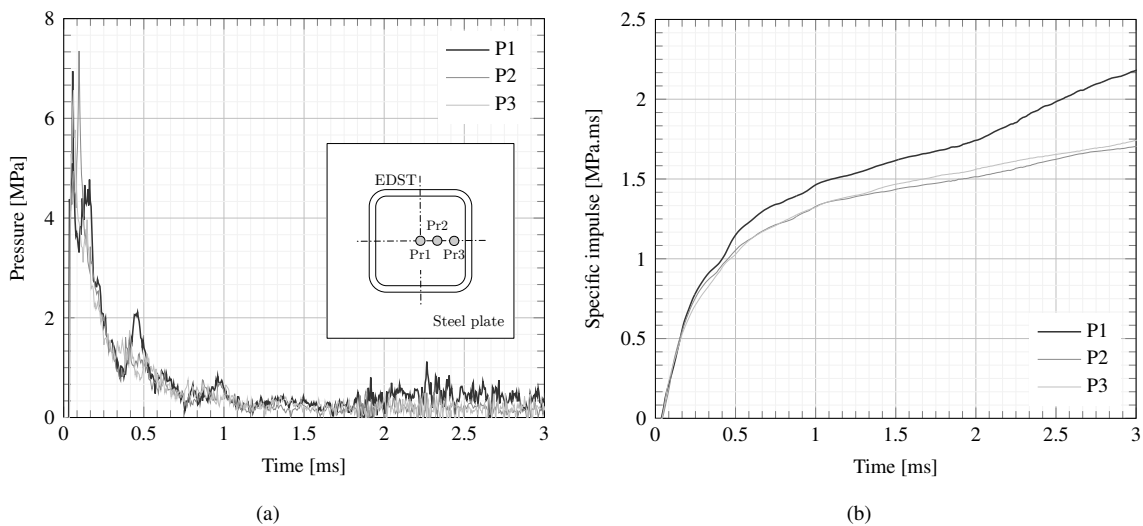

Figure 7: (a) Reflected pressure and (b) specific impulse measured at the centre of the EDST from the detonation of 50 g of C4.

Figure 8 shows a frame sequence of the blast testing of the specimen, where the failure of the bonding connection

between concrete and CFRP is visible. Although the shock tube considerably reduced the flare from the explosion, it was only possible to get clear images of the slab behaviour at approximately 8 ms after the detonation. The loss of composite action is evident since the early stages of deflection. From these images it can also be seen that at 8 ms there is already an area close to the centre of the specimen where both CFRP strips have been ripped from the slab. Although the separation starts at the centre, it propagates outwards, as shown at 12 ms.

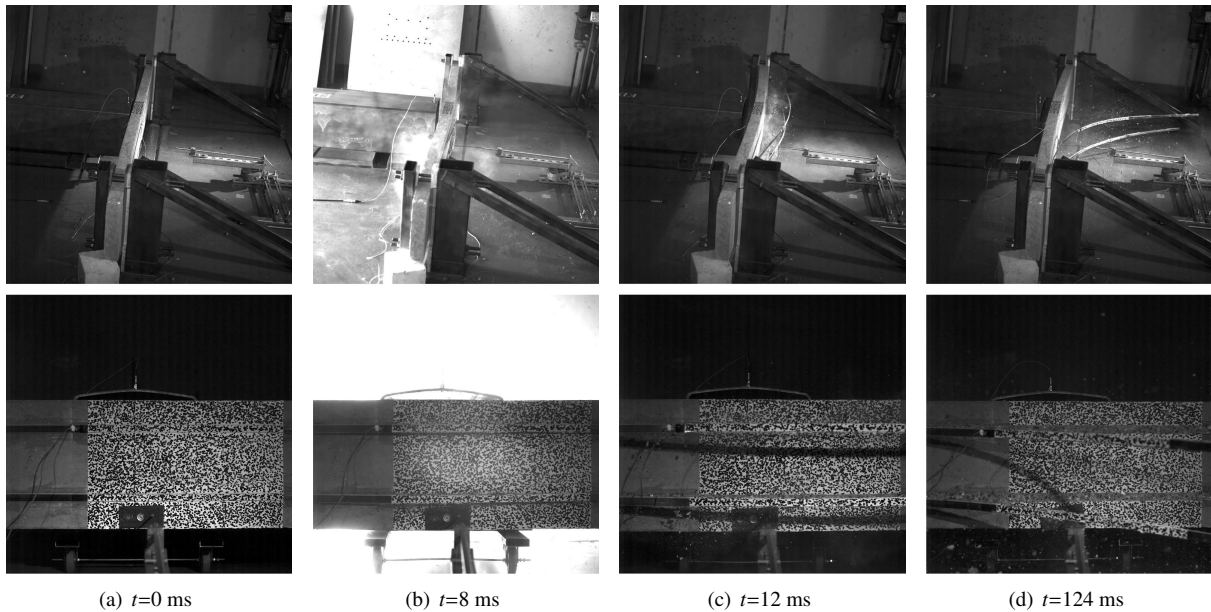(a) *t*=0 ms   (b) *t*=8 ms   (c) *t*=12 ms   (d) *t*=124 ms

Figure 8: High-speed camera footage of the blast test at different times, with debonding starting at the centre of the slab in the early stages of deflection, from approximately 8 ms onwards.

The estimation of the time at which the blast wave impinges the slab can be calculated from the side-on pressure-time history, at 20 mm from the end of the EDST, shown in Figure 9(a). Pressure measurements before $t = 0$ are due to the trigger being set at the time that the blast wave reaches the pressure transducer at the end of the tube and not at the time of detonation. Since the charge detonates inside the tube, stress waves propagate faster through the solid tube walls and reach the sensor before the actual blast wave. Pressure measurements are also different between the incident blast wave and the reverse wave reflected from the concrete surface. From the time difference between both passages of the front wave through the pressure gauge, it is possible to estimate that the structure is hit by the blast wave at approximately 0.04 ms.

The deflection-time history of the slab was recorded using a LVDT and is shown in Figure 9(b). A maximum deflection of 44 mm was registered at the centre of the slab at approximately 22 ms and the permanent deflection was found to be 5.9 mm in the direction opposite to the blast wave. During the rebound displacement, the slab impacted the shock tube, at about 43 ms, which is believed to have influenced the maximum rebound deflection.

11

The use of an explosive driven shock tube, due to the multiple reflections and superposition of shock waves, barely allows for a negative pressure phase to develop, leading to high peak pressure and a pressure-time history that is shifted upwards. Albeit, it is noteworthy to mention that in a true design case, where a free-field explosion scenario is typically considered, the negative phase might be considerable and worth including in the analysis. In such a scenario, and according to Syed *et al.* [17], while no further damage in the non-loaded face would be expected, an increased damage would be observed in the loaded surface, as a result of an increased rebound deflection. This is especially true when peak negative pressure is considerable compared to peak positive pressure.
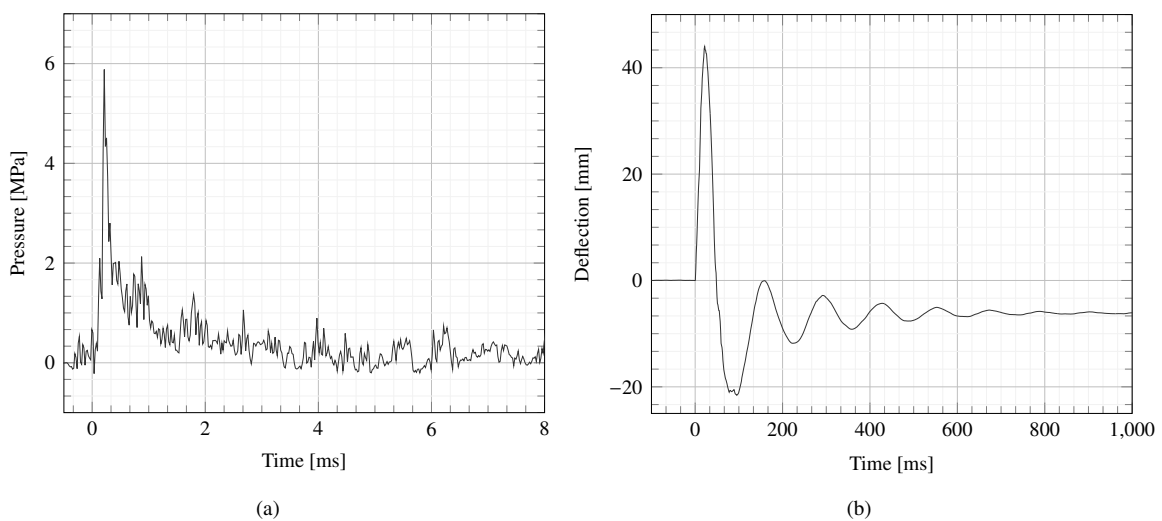

Figure 9: (a) Side-on pressure profile at 20 mm from the edges of the EDST and (b) deflection-time history of specimen B1.

The evolution of the strain on the reinforcing steel is shown in Figure 10(a), from which it is clear that steel rebars have yielded, with a strain of 0.27% (average between gauges) when the slab reached its maximum deflection, at approximately 22 ms. An initial deformation was recorded in both strain gauges prior to the strain reaching maximum deflection. Strain gauge 2 only recorded strains up to 25 ms after the trigger, which indicates its failure during testing. Nevertheless, both strain gauges present consistent data, up to the point of the failure of gauge 2, which indicates a symmetrical behaviour of the slab.

It is evident that the loss of composite action between concrete and CFRP is the main cause for structural failure, as it appeared in the very early stages of deformation of the structure. The strain gauge on the CFRP recorded a maximum strain of 0.45% at approximately 2.1 ms, when the slab presents a deflection of only 4.3 mm, as shown in Figure 10(b). This seems to indicate the initiation of CFRP disruption, followed by a sudden drop in the measured strain at 2.3 ms, which indicates the total disruption of EBR from concrete at the location where the gauge was bonded.

12
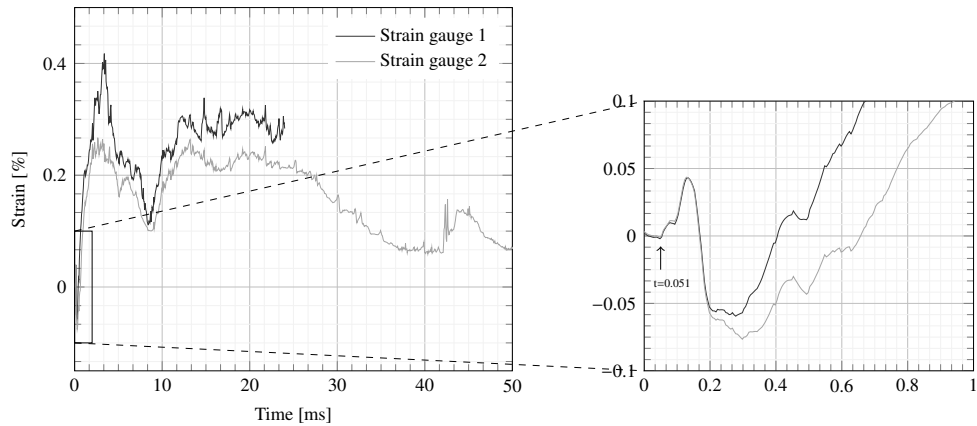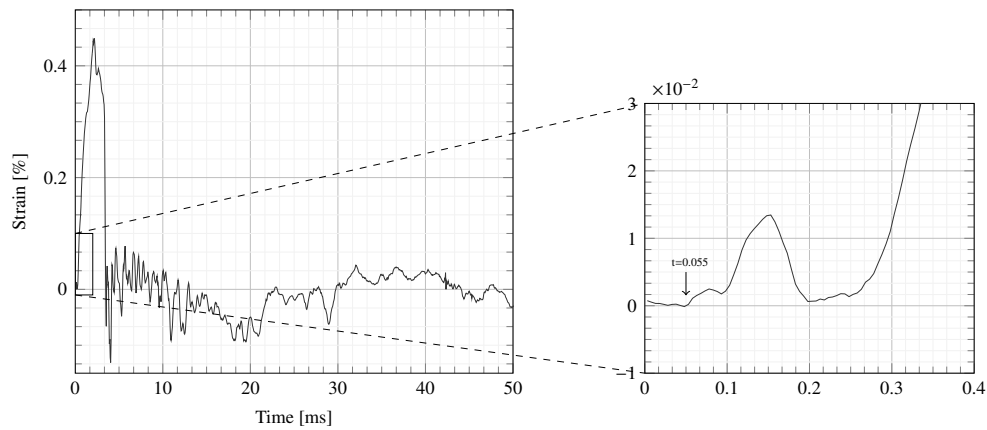
Figure 10: Strain history at the (a) tension face of the longitudinal steel rebars and (b) external face of the CRFP strips.

3. Numerical modelling

Finite element simulations of both experimental testing programs were conducted using the explicit solver LS-DYNA considering its capability in modelling both quasi-static loading and impulsive events such as blast and impact loading [18].

3.1. Quasi-static analysis

In this study, all simulations are purely Lagrangian and a general view of the model developed to simulate the quasi-static experimental testing is shown in Figure 11. The concrete was discretised using eight-node hexahedron solid elements with reduced integration (constant stress). Simulations using different mesh sizes were carried out and showed that a good compromise between accuracy and speed was obtained with an element size of approximately

13

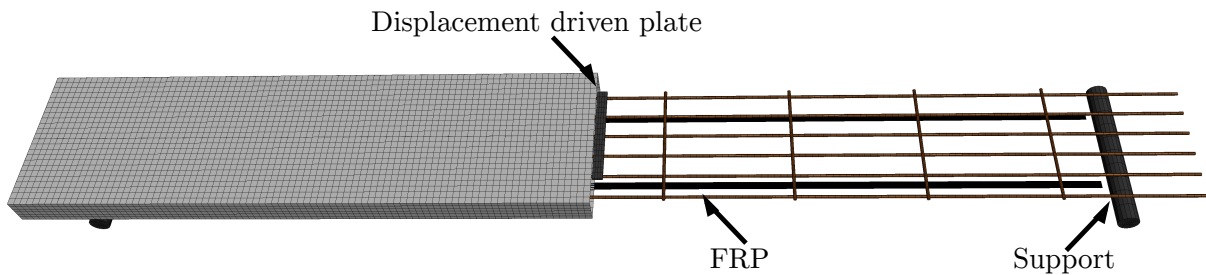10 mm, which allows the thickness to be discretised with only 6 elements.

Figure 11: Finite element model with partial cut on the right side showing CFRP and rebars.

The steel reinforcement is explicitly modelled using 10 mm beam elements with cross section integration, within the concrete mesh. The interaction between the concrete and the rebars is modelled through an interface between the two components described with the constraint method `CONSTRAINED_BEAM_IN_SOLID`, which allows an individual treatment of both components, in opposition to the commonly used smeared or shared node methods [19]. When good experimental bonding conditions are observed, neglecting relative displacement between rebars and concrete has an insignificant influence on the numerical results, reducing the risk of substantially increase the computing time [20]. CFRP strips are discretised with square 7.5 mm Belytschko-Tsay shell elements, which include an internal hourglass control algorithm [18]. Quasi-static simulations were performed using the explicit time integration method. Inertia effects, however, were minimised by applying a linearly increased displacement routine at a rate of 0.7 mm/s, which is long enough to avoid dynamic effects but not excessively long to decrease computational efficiency.

3.1.1. Material modelling

Concrete is a material that is difficult to characterise due to its history-dependent responses, heterogeneous nature, and the great influence of confinement on its properties. Although several material formulations have been implemented in finite-element solvers over the years, it has been widely reported in literature that the Karagozian & Case (K&C) concrete behaviour model is the one that better demonstrates a great capacity to match experimental data for various forms of responses, such as those emanating from quasi-static, blast, and high-velocity impact loads, as demonstrated in several studies [14, 21, 22, 23, 24, 25]. Particularly, Wu *et al.* [26] have conduct a detailed investigation on the performance of the K&C material model and addressed its behaviour in detail by comparing it to quasi-static and dynamic experimental data. The good agreement reported covers a wide range of material behaviours, such as tensile and compressive strengths, pre-peak hardening, post-peak softening, transition from brittle to ductile and higher strength under when confined, and distinct strain rates, what makes it an ideal candidate for this work.

The K&C material model is a plasticity-based model which makes use of three pressure-sensitive, independent strength surfaces to capture the variations in hardening and softening behaviours exhibited by concrete. It uses a

14

damage function to compute a failure surface on the basis of the damage imparted to the material. It also includes damage and strain rate effects, and the non-linear behaviour is represented by a cumulative effective plastic strain [27, 28]. In this model, the failure surfaces are defined as

$$\Delta\sigma_m = a_0 + \frac{p}{a_1 + a_2 p} \qquad \text{(maximum)}$$

$$\Delta\sigma_r = \frac{p}{a_{1f} + a_{2f} p} \qquad \text{(residual)} \tag{1}$$

$$\Delta\sigma_y = a_{0y} + \frac{p}{a_{1y} + a_{2y} p} \qquad \text{(yield)},$$

240 where $\Delta\sigma$ is the stress difference (on the deviatoric stress failure surface), p is the hydrostatic pressure and the

241 variables a_0, a_1 and a_2 are constants calibrated through conventional triaxial tests at different levels of confining

242 pressure. Subscripts m, r and y refer to the maximum, residual and yield shear surfaces. During the initial loading or

243 reloading, the stresses are elastic until the initial yield surface is reached, after which the material hardens or softens to

244 the maximum or residual surfaces, respectively, depending on the nature of loading. In the stress region between the

245 yield and maximum failure surfaces, the current stress is obtained by a linear interpolation between the two surfaces,

246 as

$$\Delta\sigma = \eta(\Delta\sigma_m - \Delta\sigma_y) + \Delta\sigma_y, \tag{2}$$

247 while current stress between the maximum and residual failure surfaces is linearly interpolated as

$$\Delta\sigma = \eta(\Delta\sigma_m - \Delta\sigma_r) + \Delta\sigma_r. \tag{3}$$

248 The parameter η, ranging from 0 to 1, provides the means to interpolating between the failure surfaces and is

249 function of an internal damage parameter, λ. The interpolation function $\eta - \lambda$, graphically represented in Figure 12,

250 is used by the constitutive model to represent the effects of the damage imparted to the concrete by the loading,

251 particularly related to hardening and softening. The evolution of λ arises from physical mechanisms such as internal

252 cracking due to confinement effects. For the purposes of visualization, LS-DYNA outputs the scaled damage measure

253 in a normalised form referred to as the damage index, δ, under the quantity labelled *plastic strain*. The damage index

254 is calculated as

$$\delta = \frac{2\lambda}{\lambda + \lambda_m}, \tag{4}$$

15

and equals 1 when $\lambda = \lambda_m$, signaling the arrival at the maximum failure surface. As lambda increases beyond that point, the failure surface transitions between the maximum failure surface and the residual failure surface.The arrival at the residual failure surface, indicating that concrete had softened completely, occurs when $\delta = 2$ [29].
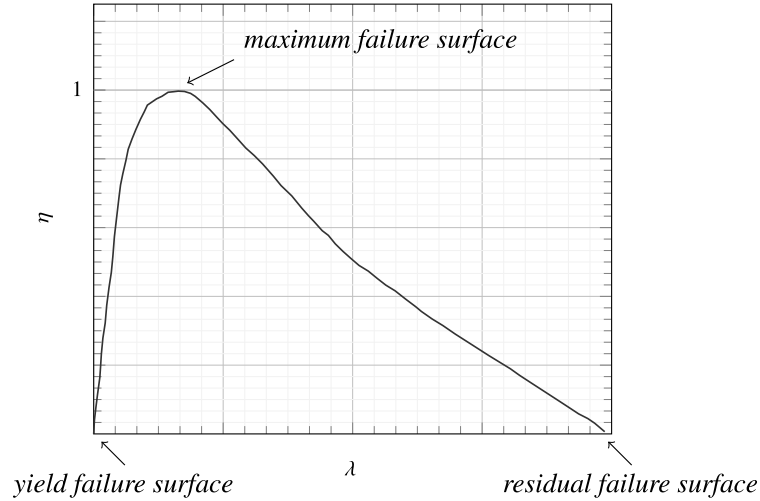

Figure 12: Failure surface interpolation function.

The model has a default parameter generation function based on the unconfined compressive strength of the concrete, which allows for a full concrete characterisation when a reduced number of properties are known. Full details of implementation of the material model can be found in references [26, 27].

The mechanical behaviour of the longitudinal rebars and transverse rods is described by an elastic-plastic material model suited to describe isotropic and kinematic hardening plasticity, with the option to use an arbitrary stress-strain curve and to include strain rate effects.

The ENHANCED_COMPOSITE_DAMAGE material model is used to describe the behaviour of the CFRP strips. This model accounts for nonlinear shear stress-strain behaviour and post-stress degradation. It also allows for the definition of the orthotropic properties of the material with multiple failure criteria, based on the Chang-Chang criterion [30], which considers compressive and tensile fibre and matrix failure. The material properties used in the FE analysis are listed in Table 3.

3.1.2. Concrete-CFRP interface

The bonding layer between the CFRP strips and the concrete volume has a thickness of only ≈ 1 mm. For this reason, it was decided to avoid explicitly modelling this layer as it would compromise the computational cost of the simulations, without a clear benefit to the results. Instead of implementing a macroscopic bond stress slip relation through the use of cohesive elements, a simpler approach using a tiebreak contact algorithm was implemented. A

16

Table 3: Material properties used in the finite element model [4, 31].

Concrete	
Unconfined compressive strength [MPa]	50.1
Density [kg/m^3]	2,400
Steel	
Density [kg/m^3]	7,800
Poisson's ratio	0.3
Young's modulus [GPa]	207
Yield strength [MPa]	500
CFRP	
Density [kg/m^3]	1,600
Poisson's ratio	0.021
Young's modulus, major axis [GPa]	165
Shear modulus [MPa]	5,000
Tensile strength [MPa]	3,100

strength-based interface was defined, according to which the separation of initially tied surfaces is initiated when a prescribed failure criterion described by

$$\left(\frac{|\sigma_n|}{\sigma_{NF}}\right)^2 + \left(\frac{|\sigma_s|}{\sigma_{SF}}\right)^2 \geq 1 \tag{5}$$

is met, where σ_n and σ_s are the normal and shear stresses at the interface surface, and σ_{NF} and σ_{SF} are the corresponding tensile and shear stresses at failure, respectively. After failure, further contact between the surfaces is treated as a simple compression interface and no tension is considered.

A number of authors have defined σ_{NF} and σ_{SF} based on the normal tensile and shear stress of the epoxy at failure [14, 32, 33, 34]. It has, however, become clear from the experimental results that failure occurs at the concrete substrate and not at the epoxy layer, which was expected due to the lower mechanical properties of concrete under tensile and shear stresses. These failure stresses should be estimated from either pull-out testing of the two tied materials or validated through empirical models. The tensile shear stress σ_{NF} is defined as

$$\sigma_{NF} = 0.3 f_c^{2/3}, \tag{6}$$

where f_c is the compressive strength of concrete [35]. The shear stress at failure is estimated as

$$\sigma_{SF} = 1.5\beta_w\sigma_{NF} \tag{7}$$

with

$$\beta_w = \sqrt{\frac{2.25 - b_f/b_c}{1.25 + b_f/b_c}}, \tag{8}$$

where b_f/b_c is the FRP laminate-to-concrete width ratio [36].

3.1.3. Validation and results

The load-deflection results are shown in Figure 13, where an overall good agreement between numerical and experimental data for both the control and retrofitted specimens can be observed. For the control specimen, the numerical model presents an initial higher stiffness, which can be explained by the reduced thickness of the slab, which induced the formation of micro cracks from drying shrinkage in the concrete or handling. The same was not observed in the test with CFRP, where the stiffness of the composite material plays a major role. The formation of a plastic hinge and the post-peak softening stage are visible on the control specimen and are well captured by the numerical model, as can be seen in Figure 13(a). A similar behaviour was observed in the strengthened slab, Figure 13(b), where the numerical model presents a similar cracking stage stiffness and a good prediction of the damage phase, after the formation of a plastic hinge. The numerical model is efficient in predicting CFRP debonding as well, which validates the numerical approach to represent the detachment process as well as the estimation of the interfacial shear and normal stresses at failure. These observations indicate that in general, the proposed numerical model is able to replicate the recorded data.
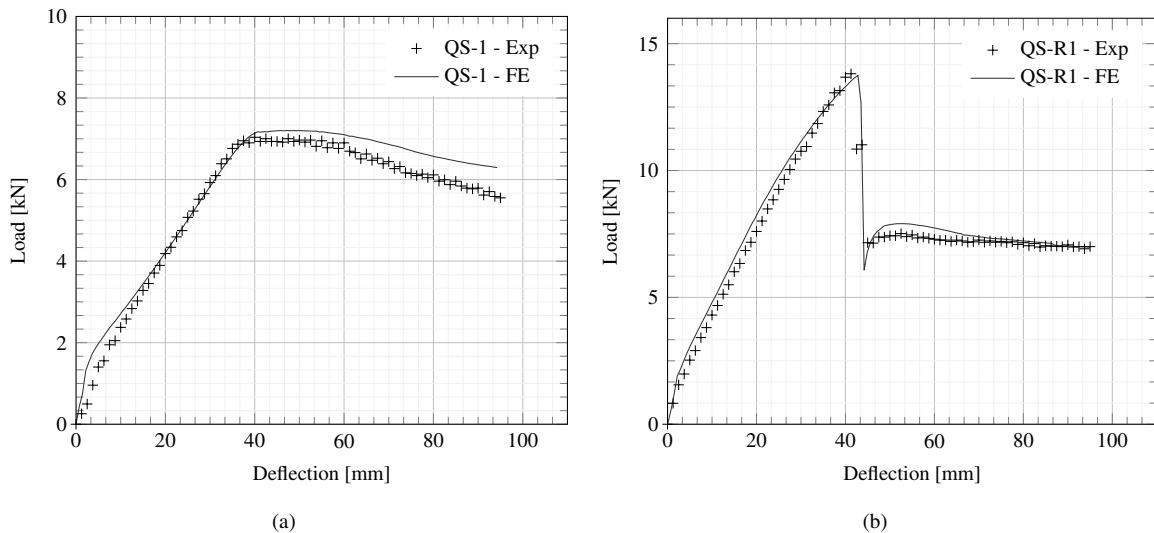

Figure 13: Experimental and numerical load-deflection results for specimens (a) QS-1 and (b) QS-R1.

Although the K&C material model does not provide predictions of crack patterns and their location, that can be

addressed by the quantity labeled effective plastic strain, representing the internal damage index, δ. Figure 3.1.3 depicts the accumulated damage over the span for different displacement stages. It can be seen that although flexural damage starts to develop along the span, its maximum value occurs at the mid-span, where $\delta \approx 2$, reaching the point where a plastic hinge develops in the tension side of the specimen and concrete crushing initiates on the loaded side. Such results indicate a good match with the experimental results presented in Figure 3, indicating the accurateness of the numerical predictions.
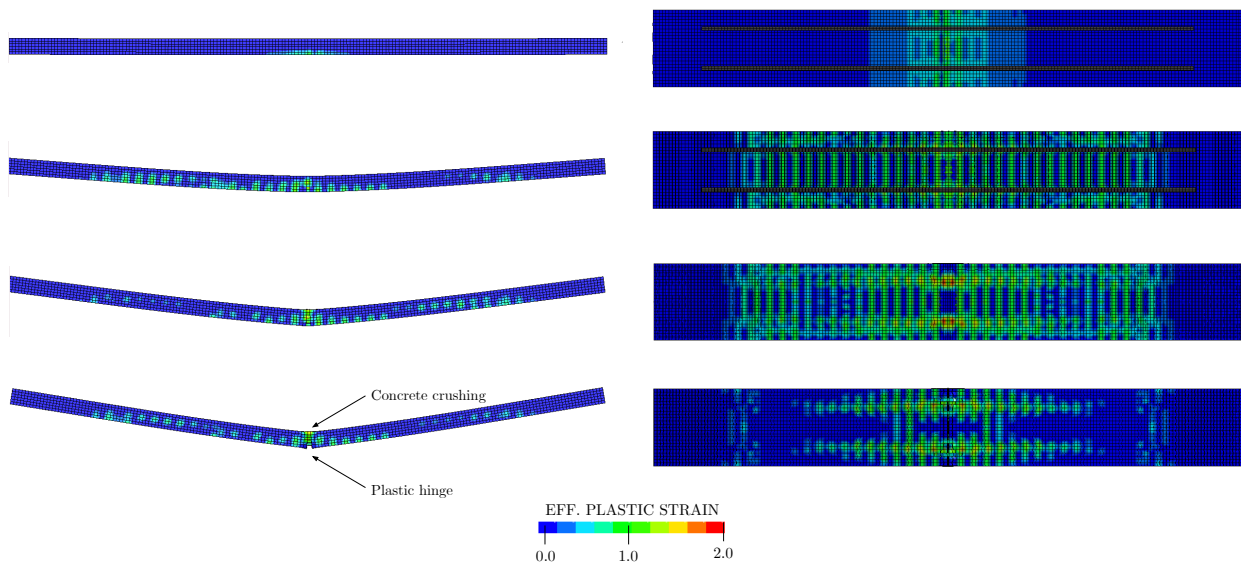
prediction of damage distribution over the span for different displacement stages of the quasi-static testing, and evidence of CFRP disruption.

Despite strains in the CFRP not being measured in the quasi-static experimental testing, the numerical model allows for their prediction. Strains along the length of the CFRP are shown in Figure 14, for different values of mid-span deflection, corresponding to different load levels. As expected, due to the bonding interface and strain compatibility, strain increases proportionally to the deflection, reaching its maximum value at mid-span. The spaced dash-dotted line illustrates the ultimate deflection before the disruption of the EBR from concrete, meaning that the ultimate mid-span strain in the CFRP was 0.53%.

Figure 15 shows a sequence of frames of the concrete-CFRP interface for different deflection levels, illustrating the propagation of debonding. Although total debonding took place when the slab presented a mid-span deflection of 43.1 mm, small debonded areas started to be visible from a mid-span deflection of 31.8 mm, later propagating towards the supports (areas in red indicate debonding). This observation is consistent with findings presented in the literature, which indicate that one of the possible concrete-CFRP interface failure modes under quasi-static loading is intermediate crack induced debonding [37, 38, 39]. Although this failure mode is less common than debonding at the

CFRP end due to shear failure of concrete, it seems to be the case for the tested specimens due to their slenderness and, hence, shear failure is not of a concern. Additionally, the appearance of this specific failure mode might also be attributed to the test configuration. Normally RC slabs are tested in four-point bending, where propagation of debonding within the constant moment region does not change the stress distribution within the strengthened system, since it is not energetically justified. However, as the current test setup lies on a three-point bending configuration, which does not induce a constant moment region, it is possible that the high interfacial shear stress concentrations around flexural cracks may be the cause of debonding and its propagation towards the supports, as schematically represented in Figure 16.
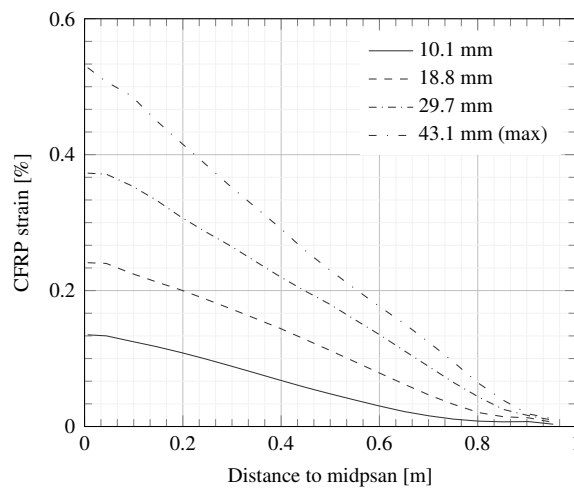

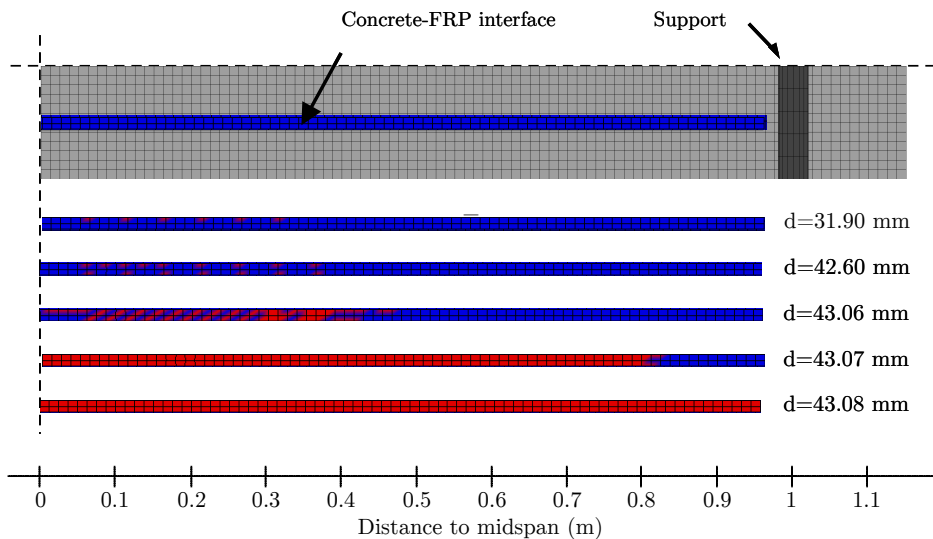Figure 14: Numerical prediction of the distribution of strain in CFRP, for different mid-span deflection levels.

Figure 15: Bottom view of a quarter of the slab with numerical prediction of debonding at different deflection levels.
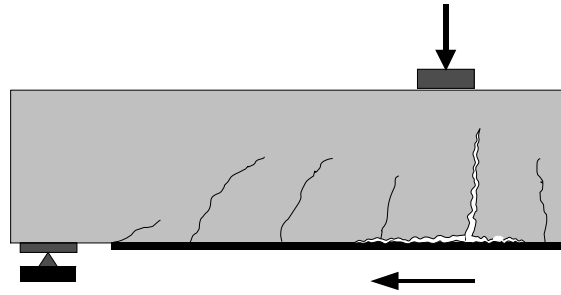
20

Figure 16: Schematic representation of the intermediate crack induced debonding failure mode (adapted from [40]).

3.2. Blast analysis

Model discretisation, constitutive models and the modelling of interfaces are similar to those used in the quasi-stating modelling. To estimate the correct behaviour of the specimen, however, it is imperative that the full setup is modelled as the experimental setup does neither represent a fully clamped nor a simply-supported configuration, leading to the need of realistically representing the setup without simplifications. Figure 17 shows the numerical model used to simulate the blast testing. Metallic supports are represented by Belytschko-Tsay shell elements, and eight-node hexahedron solid elements are used to describe the wood and rubber sheets. The explosive driven shock tube is included as well, due to its interference in the rebound phase of the slab oscillation. Dynamic increase factors (DIF) are used to scale material properties to their dynamic range, as described in Section 3.2.1.

(a)

(b)
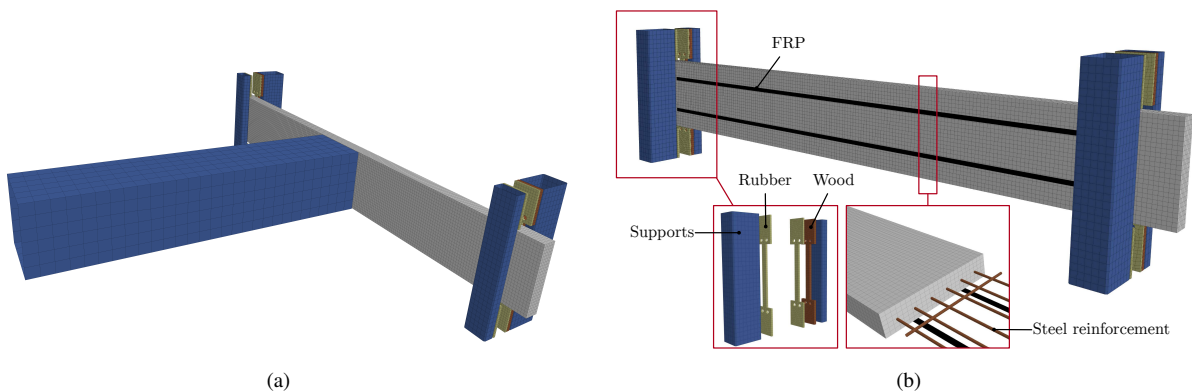
Figure 17: (a) Overview of the numerical model used to represent the experimental setup and (b) detailed view of supports and steel reinforcement.

An empirical blast pressure is applied on the face of the concrete volume instead of modelling the high explosive and its detonation. This is justified by the blast wave planarity observed experimentally with the EDST. An idealised triangular ramp pressure time history is defined to simulate the experimental pressure pulse. This pulse has the same peak overpressure as the experimental measurements and its duration is calculated to ensure a similar specific impulse. The constitutive behaviour of the rubber sheets in the supports is described by the uniparameter material model

21

`MAT_BLATZ-KO_RUBBER`, which allows to model the properties of low-compressibility solid materials. The Piola-Kirchhoff stress, the relative volume, defined as the ratio of the current volume to the initial volume, and the right Cauchy-Green strain tensor are automatically generated [41]. The Poisson's ratio is $\nu = 0.463$ [29].

3.2.1. Strain Rate Effects

Blast loads typically induce very high strain rates, leading to completely different material behaviour compared to their quasi-static response. In the present work, strength enhancement under high loading rate conditions is accounted for by dynamic increase factors, which are calculated as the ratio of the dynamic to the static material strength [42]. For average strength concrete, with compressive strengths ranging from 20 to 70 MPa, the most comprehensive model for strain rate enhancement is described by FIB as

$$\text{DIF} = \frac{f_c}{f_{c0}} = \left(\frac{\dot{\varepsilon}_c}{\dot{\varepsilon}_{c0}}\right)^{0.014} \quad \text{for} \quad \dot{\varepsilon}_c \leq 30 \text{ s}^{-1}$$

$$\text{DIF} = \frac{f_c}{f_{c0}} = 0.012\left(\frac{\dot{\varepsilon}_c}{\dot{\varepsilon}_{c0}}\right)^{\frac{1}{3}} \quad \text{for} \quad \dot{\varepsilon}_c > 30 \text{ s}^{-1}, \tag{9}$$

where f_c is the dynamic compressive strength at strain rate $\dot{\varepsilon}_c$; f_{c0} is the static compressive strength at strain rate $\dot{\varepsilon}_{c0}$, $\dot{\varepsilon}_c$ is the dynamic strain rate and $\dot{\varepsilon}_{c0} = 30 \times 10^{-6}$ [35]. In tension, the DIF for the strength of concrete is

$$\text{DIF} = \frac{f_t}{f_{t0}} = \left(\frac{\dot{\varepsilon}_t}{\dot{\varepsilon}_{t0}}\right)^{0.018} \quad \text{for} \quad \dot{\varepsilon}_t \leq 10 \text{ s}^{-1}$$

$$\text{DIF} = \frac{f_c}{f_{c0}} = 0.0062\left(\frac{\dot{\varepsilon}_t}{\dot{\varepsilon}_{t0}}\right)^{\frac{1}{3}} \quad \text{for} \quad \dot{\varepsilon}_t > 10 \text{ s}^{-1}, \tag{10}$$

where f_t is the dynamic tensile strength at strain rate $\dot{\varepsilon}_t$ and f_{t0} the static tensile strength at strain rate $\dot{\varepsilon}_{t0} = 10^{-6}$ [35]. DIF values for the specific concrete used in this work are shown in Figure 18.

Strain rate effects in steel are accounted for by the Cowper-Symonds model [18], which scales the yield stress by a strain rate dependent factor, as

$$\sigma_y = \sigma_0 \left[1 + \left(\frac{\dot{\varepsilon}}{C}\right)^{\frac{1}{p}}\right], \tag{11}$$

where σ_0 is the yield stress under static loading, $\dot{\varepsilon}$ is the current strain rate and $C = 40 \text{ s}^{-1}$ and $p = 5$ are the strain rate parameters, as presented by Jia *et al.* [43]. The strain rate strength enhancement of CFRP is not considered in this study due to its insignificance when compared to concrete and steel, as shown by the experimental results presented by Kimura *et al.* [44], who have tested a series of unidirectional CFRP specimens at different strain rates and observed no influence in the tensile strength.
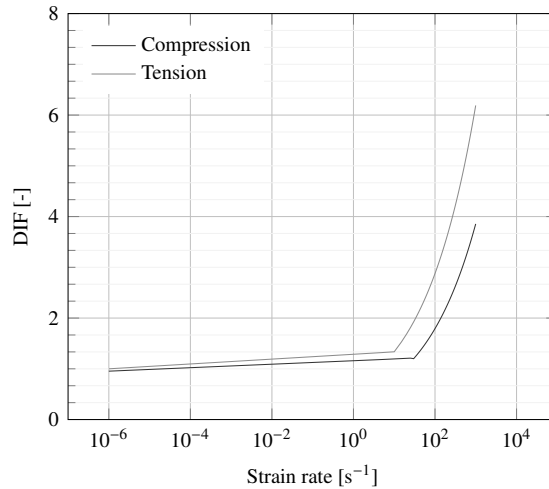
Figure 18: Strain rate effect on the compressive and tensile strength of concrete.

3.2.2. Validation and results

Additional experimental testing conducted by Maazoun *et al.* [4] was used to calibrate the FE model developed in this study. In their study, the authors investigated the effectiveness of CFRP strips on the load bearing capacity of reinforced concrete one-way slabs under blast loading, in situations where debonding is not an issue. For that, the explosive charge was selected so that loss of composite action between concrete and CFRP is not an issue. The setup and specimens used by the authors were the same as those of the present work. To calibrate and validate the numerical models developed in this work, the control specimen and the specimen with two strips, specimens A1 and A3, respectively, are used as benchmark. Noting that the main goal is to validate the use of material models under blast loading, and since the authors did not observe any detachment of the CFRP strips, a full bond connection is used in the model validation simulations. While such assumption is made for validations purposes, based on experimental observations, interface failure is also included in the prediction of the experimental results presented above. Discussion on the behaviour of the bond interface is presented later.

The experimental deflection-time histories by Maazoun *et al.* [4] and the correspondent numerical predictions for specimens A1 and A3 are shown in Figures 19(a) and 19(b), respectively. As can be seen, both the control and the retrofitted specimens present a good correlation with experimental data not only on the prediction of maximum displacement and time to maximum displacement, but also on the overall time history. While for specimen A1 the FE model is capable of capturing both inbound and rebound deflections well, the same behaviour cannot be compared for specimen A3 due to lack of experimental data after the first inbound deflection. Experimental observations and numerical predictions for all specimens are listed in Table 4.

To better validate the numerical model, a comparison of the overall damage observed by Maazoun *et al.* [4] and

23

Table 4: Experimental observations and numerical results for all specimens: mid-span deflection, maximum strain in steel rebars and maximum strain in CFRP.

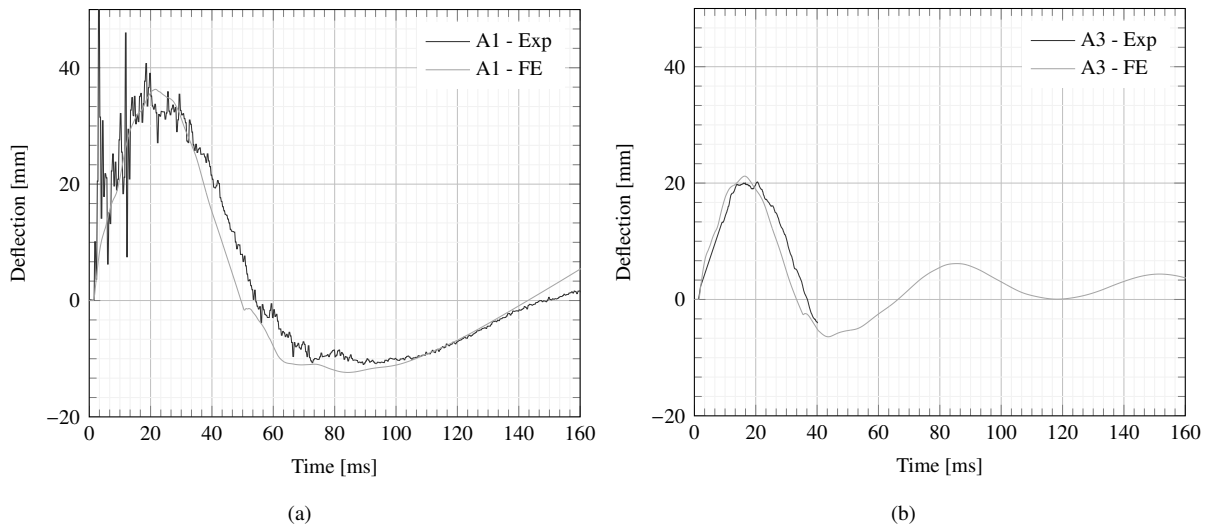| Slab ID	Mid-span deflection (mm)			Maximum strain steel (%)			Maximum strain CFRP (%)		
	EXP	FEM	EXP/FEM	EXP	FEM	EXP/FEM	EXP	FEM	EXP/FEM
A1	34.2	36.3	0.94	0.34	0.33	1.03	–	–	–
A3	20.0	21.2	0.94	0.18	0.20	0.90	0.25	0.26	0.96
B1	44.0	44.8	0.98	0.27	0.24	1.12	0.45	(0.03)	(15.0)

(a)

(b)

Figure 19: Deflection-time comparison between experimental and numerical results for (a) specimen A1 and (b) specimen A3.

numerical predictions is presented in Figure 20(a) and (b). Assuming the damage correspondence of the effective plastic strain, distribution of cracks over the span of both specimens A1 and A3 is overall well predicted. Particularly, in the case of specimen A3, the numerical model is able to predict an higher density of cracks in the loaded side, resultant from the amplified rebound effect due to the release of elastic energy stored in the FRP following the inbound displacement. Similarly, the FE model of specimen A1 presents an even distribution of cracks in both the loaded and non-loaded surfaces, as well a good prediction of the number of cracks and its spacing.

Comparison between the strain histories in the longitudinal steel bars and experimental observations is shown in Figures 21(a) and 21(b) for specimen A1 and A3, respectively, whilst Figure 21(c) shows the comparison for the strain in the CFRP. Overall, the first strain peak is well predicted at $t = 4$ ms for all measurements, corresponding to the local deformation due to the shock wave propagation within the material. Good agreement is also obtained at approximately 22 and 18 ms for the control and the retrofitted specimens, respectively, corresponding to the deformations caused by the bending behaviour of the slab (at the time of maximum deflection). Yet, after the first strain peak, it is observed that the numerical predictions tend to be constantly shifted in time when compared to the experimental data. This is

24

Non-loaded side

Loaded side

(a)

Non-loaded side

Loaded side

EFF. PLASTIC STRAIN
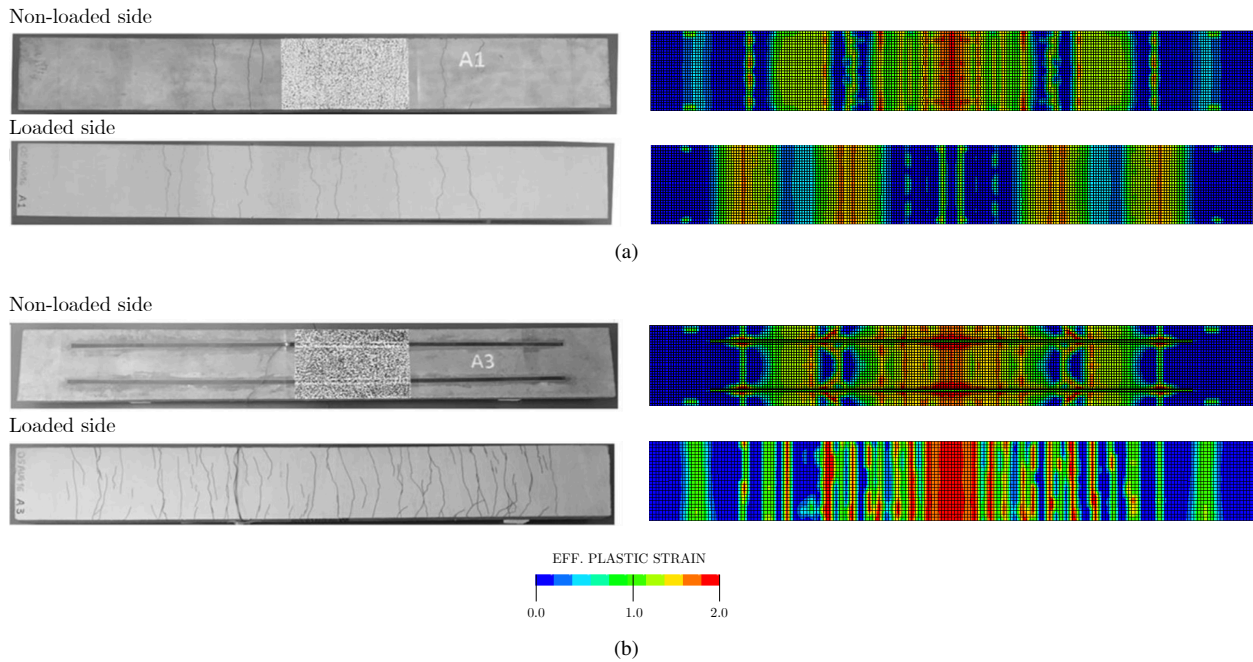
0.0   1.0   2.0

(b)

Figure 20: Comparison between crack distributions observed by Maazoun *et al.* [4] and corresponding numerical predictions for (a) specimen A1 and (b) A3.

mainly caused by the modelling assumption of perfect bond between the concrete volume and the steel rebars, and between the concrete and the CFRP.

To understand how the model predicts the response of the slab when the dynamic disruption of the EBR needs to be taken into account, the numerical model is again used and compared against the experimental observations from specimen B1, presented in Section 2.4. Since the disruption of the EBR is of interest, the modelling technique used to replicate debonding under quasi-static modelling is also used under blast loading.

Figure 22(a) shows a comparison between the computed and experimental mid-span deflection-time histories. The predicted maximum deflection is 44.8 mm, which is in close agreement with the maximum test value of approximately 44 mm. Although the the FE model predicts well the first inbound deflection and both the time to maximum deflection and the return time to the initial position, the model underestimates the maximum rebound deflection. Strains in the steel, as shown in Figure 22(b), corroborate the ability of the model to correctly represent the behaviour of the slab during the first deflection. It can be seen that both the first strain peak and the peak correspondent to maximum deflection correlate well with the test data. When analysing the results in terms of strain on the CFRP, however, the model does not deform significantly before rupture, which occurs immediately after the load application, in contrast with the experimental results. Such behaviour can be explained by the simplified interface modelling technique used, which is based on a tie-break contact approach. As this method relies on shear and normal stress thresholds

25

to release the bonded interface, which were calibrated with quasi-static results, it does not account for the stress wave propagation and concrete failure to which the dynamic excitation of the structure leads. A better modelling of the failure mechanism could be achieved by implementing element erosion techniques. However, these rely on extremely refined finite element discretisations, which would lead to significant increases in computational times and, consequently, computational cost.

Figure 23 depicts the experimental crack locations in specimen B1 along with the corresponding numerical predictions. For the sake of clarity, regions of the numerical model with $\delta \geq 1.8$ are highlighted, indicating the predicted location of crack initiation. As shown, there is a higher concentration of cracks in the non-loaded side of the specimen, mainly located around the mid-span. On the other hand, the loaded side of the specimen shows a lower crack density, mainly located towards the end of the specimen. This is consistent with the experimental observations and reveals the accuracy of the numerical model in predicting the damage imparted to concrete due to blast loading, in addition to an accurate prediction of its flexural behaviour.

4. Discussion

This study analyses the effect of loading time, from quasi-static to impulsive, on the behaviour of RC slabs with externally bonded CFRP, with particular focus on the debonding mechanism.

The location and failure mode of the bonded interface is consistent for both the quasi-static and the blast loading, being characterised by the failure of the concrete substrate in the vicinity of the epoxy layer, with no damage imparted to the CFRP strips. According to Figures 10(b) and 14, the maximum strain in the CFRP is 0.45 and 0.53% under dynamic and quasi-static conditions, respectively. Acknowledging that CFRP behaves linearly elastic up to the point of rupture (elongation at break is 1.6%, according to the manufacturer [45]), it is clear that no damage is imparted to the CFRP due to the blast loading. The physical mechanism that leads to the concrete failure under the diferent loading conditions is, however, divergent. Under quasi-static conditions, total debonding takes place at a deflection level of 42 and 52 mm, for specimens QS-1 and QS-2, respectively, while under blast loading it takes place at the very early stages of loading, when the slab has only deflected 4.5 mm, represented by the abrupt decay in the strain measured in the CFRP.

Disruption of EBR from quasi-static testing is caused by flexural cracks that induce strong gradients of interfacial shear stress and promotes its initiation and propagation. By contrast, strain measurements in the CFRP during blast testing imply that the separation of the CFRP from the concrete is initiated by the propagation of stress waves within the material. This is further supported by the time taken for the stress wave to travel between strain gauges. Considering that the wave speed is $c = \sqrt{E/\rho}$, where E and ρ are the Young's modulus and density of the propagation

medium [46], respectively, and that the steel rebars and the extreme fibre of the CFRP are located at 43 and 63.5 mm from the surface of the slab, respectively, it takes 8.7 and 13.2 μs for the stress wave to travel from the front surface of the slab to the strain gauge on the steel rebars and on the CFRP, respectively. As the blast wave impinges the slab at $t = 40\,\mu$s, the strain peaks corresponding to $t = 51\,\mu$s in Figure 10(a) and $t = 55\,\mu$s in Figure 10(b) are consistent with the calculated stress wave arrival times. Additionally, the CFRP strain signal returns to zero immediately after the first peak, at $t = 150\,\mu$s, which is consistent with the stress reversal behaviour of elastic waves at free interfaces. When a compressive stress wave travelling within a material finds a free interface, it is reflected as a tensile wave of the same magnitude. This is visible from the strain measured on the steel, where a negative pulse, after the arrival of the first compressive wave, develops due to the superposition of reflected tensile waves from the subsequent interfaces: concrete-epoxy, epoxy-CFRP and free interface. Prior to the rapid propagation of the stress wave and the relative small strains measured on the reinforcing steel, a considerable strain peak is observed at $t = 2.5$ ms, related to the energy transferred from the blast to the components which induce deformation ahead of structural deflection. This also applies to the behaviour of the CFRP where, due to the transfer of momentum, inertial forces develop and pull the CFRP from the concrete substrate until rupture occurs at the location of the strain gauge, with a maximum strain of 0.45%. It should be noted that, under quasi-static conditions, the disruption of the CFRP (at 0.1 m from mid-span) is associated to a maximum strain of 0.48%, as can be seen in Figure 15. The results indicate a similar strain dependency in the CFRP debonding mechanism, although different types of loading and structural responses are present.

The good agreement between experimental observations and numerical results described above indicates that the stress wave propagation in the material combined with the momentum transmitted to the CFRP are the main causes of concrete fracture and of the initiation of debonding under dynamic conditions. The modelling technique used to represent the rupture of the EBR, however, does not provide accurate results under dynamic conditions when the failure criteria of the contact algorithm is based on empirical strength models. The CFRP does not develop considerable strain until disruption occurs, which might be explained by the different concrete-to-CFRP interface failure trigger described above, when comparing quasi-static to blast conditions, that is not captured by the simplified interface modelling technique. Nevertheless, it does not seem to affect neither the numerically predicted displacement nor the strain profile of the reinforcing steel, as supported by the results in Figures 22(a) and 22(b). This might indicate that although the CFRP stayed in place until the later stages of the test it played a minimal role on the overall structural response of the slab, which is in accordance with the observations of Maazoun *et al.* [47]. The authors concluded that the maximum deflection of a slab reinforced with externally bonded CFRP is the same as a control specimen if the magnitude of the blast load is sufficient to induce the disruption of the CFRP.

5. Concluding remarks

In this study, the influence of externally bonded CFRP strips on one-way reinforced concrete slabs under quasi-static and blast loading has been investigated both experimentally and numerically. Based on the study results, the following conclusions can be drawn:

- Under quasi-static loading, the use of CFRP as external bonded reinforcement increased the maximum displacement before failure by 18% and the maximum load carrying capacity by 115%, compared to the control specimen.

- The failure of the CFRP-to-concrete interface is caused by the failure of concrete in the vicinity of the interface, mostly due to concentration of interfacial shear stresses around mid-span flexural cracks that propagate towards the supports, as shown by the FE results.

- The quasi-static FE model is capable of simulating the load-deformation characteristics of the structure and the CFRP-to-concrete bond, accurately predicting the interface disruption and post-debonding residual capacity.

- The experimental blast testing provided insights on the mechanism that leads to the disruption of the EBR. The strain on the steel rebars and CFRP indicates that stress wave propagation through the thickness of the specimen combined with momentum transfer to CFRP are the main reason for the rupture under dynamic conditions.

- By comparing the set of quasi-static and dynamic results it was found that although the bonded interface failure mechanism differs, the CFRP shows similar longitudinal strain when disruption takes place, indicating a strain dependency on the interface failure.

References

[1] C. Wu, D. Oehlers, M. Rebentrost, J. Leach, A. Whittaker, Blast testing of ultra-high performance fibre and FRP-retrofitted concrete slabs, Engineering Structures 31 (9) (2009) 2060–2069. doi:10.1016/j.engstruct.2009.03.020.

[2] J.-H. Ha, N.-H. Yi, J.-K. Choi, J.-H. J. Kim, Experimental study on hybrid CFRP-PU strengthening effect on RC panels under blast loading, Composite Structures 93 (8) (2011) 2070–2082. doi:10.1016/j.compstruct.2011.02.014.

[3] S. L. Orton, V. P. Chiarito, J. K. Minor, T. G. Coleman, Experimental Testing of CFRP-Strengthened Reinforced Concrete Slab Elements Loaded by Close-In Blast, Journal of Structural Engineering 140 (2) (2014) 04013060. doi:10.1061/(ASCE)ST.1943-541X.0000821.

[4] A. Maazoun, S. Matthys, B. Belkassem, D. Lecompte, J. Vantomme, Experimental Analysis of CFRP Strengthened Reinforced Concrete Slabs Loaded by Two Independent Explosions, Proceedings 2 (8) (2018) 436. doi:10.3390/ICEM18-05317.

[5] A. G. Razaqpur, A. Tolba, E. Contestabile, Blast loading response of reinforced concrete panels reinforced with externally bonded GFRP laminates, Composites Part B: Engineering 38 (5-6) (2007) 535–546. doi:10.1016/j.compositesb.2006.06.016.

[6] J. E. Crawford, L. J. Malvar, B. W. Dunn, D. J. Gee, Retrofit of Reinforced Concrete Columns Using Composite Wraps to Resist Blast Effects, Tech. Report, Karagozian & Case, California (1996).

[7] Y. Shi, H. Hao, Z.-X. Li, Numerical derivation of pressure–impulse diagrams for prediction of RC column damage to blast loads, International Journal of Impact Engineering 35 (11) (2008) 1213–1227. `doi:10.1016/j.ijimpeng.2007.09.001`.

[8] H. Elsanadedy, T. Almusallam, H. Abbas, Y. Al-Salloum, S. Alsayed, Effect of blast loading on CFRP-Retrofitted RC columns - a numerical study, Latin American Journal of Solids and Structures 8 (1) (2011) 55–81. `doi:10.1590/S1679-78252011000100004`.

[9] A. A. Mutalib, H. Hao, Development of P-I diagrams for FRP strengthened RC columns, International Journal of Impact Engineering 38 (5) (2011) 290–304. `doi:10.1016/j.ijimpeng.2010.10.029`.

[10] M. Abedini, A. A. Mutalib, S. Baharom, H. Hao, Reliability Analysis of P-I Diagram Formula for RC Column Subjected to Blast Load, International Journal of Civil and Environmental Engineering 7 (8) (2013) 5.

[11] X. Lin, Y. X. Zhang, Nonlinear Finite Element Analysis of FRP-Strengthened Reinforced Concrete Panels Under Blast Loads, International Journal of Computational Methods 13 (04) (2016) 1641002. `doi:10.1142/S0219876216410024`.

[12] A. A. Mutalib, H. Hao, Development of P-I diagrams for FRP strengthened RC columns, International Journal of Impact Engineering 38 (5) (2011) 290–304. `doi:10.1016/j.ijimpeng.2010.10.029`.

[13] G. Pezzola, L. Stewart, G. Hegemier, Analysis methods for CFRP blast retrofitted reinforced concrete wall systems, International Journal of Computational Methods and Experimental Measurements 4 (3) (2016) 247–257. `doi:10.2495/CMEM-V4-N3-247-257`.

[14] A. Maazoun, S. Matthys, B. Belkassem, D. Lecompte, J. Vantomme, Blast response of retrofitted reinforced concrete hollow core slabs under a close distance explosion, Engineering Structures 191 (2019) 447–459. `doi:10.1016/j.engstruct.2019.04.068`.

[15] X. H. Zheng, P. Y. Huang, X. Y. Guo, J. L. Huang, Experimental Study on Bond Behavior of FRP-Concrete Interface in Hygrothermal Environment, International Journal of Polymer Science 2016 (2016) 1–12. `doi:10.1155/2016/5832130`.

[16] H. Ousji, B. Belkassem, M. A. Louar, D. Kakogiannis, B. Reymen, L. Pyl, J. Vantomme, Parametric Study of an Explosive-Driven Shock Tube as Blast Loading Tool, Experimental Techniques 40 (4) (2016) 1307–1325. `doi:10.1007/s40799-016-0128-3`.

[17] Z. I. Syed, P. Mendis, S. A. Rahman, Effect of Large Negative Phase of Blast Loading on Structural Response of RC Elements, MATEC Web of Conferences 47 (2016) 02015. `doi:10.1051/matecconf/20164702015`.

[18] Livermore Software Technology Corporation, LS-DYNA User Manual: Volume I (Version R10.0), California (2017).

[19] L. Schwer, Modeling rebar: The forgotten sister in reinforced concrete modelling, Tech. Report, Schwer Engineering & Consulting Services (2014).

[20] P. Grassl, M. Johansson, J. Leppanen, On the numerical modelling of bond for the failure analysis of reinforced concrete, Engineering Fracture Mechanics 189 (2017) 13–26. `doi:10.1016/j.engfracmech.2017.10.008`.

[21] J. E. Crawford, Y. Wu, J. M. Magallanes, S. Lan, Modeling of concrete materials under extreme loads, in: Advances in Protective Structures Reseaerch, 1st Edition, Taylor and Francis, London, 2012, p. 32.

[22] J. E. Crawford, State of the art for enhancing the blast resistance of reinforced concrete columns with fiber-reinforced plastic, Can. J. Civ. Eng. 40 (11) (2013) 1023–1033. `doi:10.1139/cjce-2012-0510`.

[23] Y. Wu, J. E. Crawford, S. Lan, J. M. Magallanes, Validation Studies for Concrete Constitutive Models with Blast Test Data, in: 13th International LS-DYNA Users Conference, Dearborn, MI, 2014, p. 12.

[24] A. Mardalizad, M. Caruso, A. Manes, M. Giglio, Investigation of mechanical behaviour of a quasi-brittle material using Karagozian and Case concrete (KCC) model, Journal of Rock Mechanics and Geotechnical Engineering 11 (6) (2019) 1119–1137. `doi:10.1016/j.jrmge.2019.01.005`.

[25] W. Feng, B. Chen, F. Yang, F. Liu, L. Li, L. Jing, H. Li, Numerical study on blast responses of rubberized concrete slabs using the Karagozian

and Case concrete model, Journal of Building Engineering 33 (2021) 101610. doi:10.1016/j.jobe.2020.101610.

[26] Y. Wu, J. E. Crawford, Numerical Modeling of Concrete Using a Partially Associative Plasticity Model, J. Eng. Mech. 141 (12) (2015) 04015051. doi:10.1061/(ASCE)EM.1943-7889.0000952.

[27] L. Malvar, J. E. Crawford, J. W. Wesevich, D. Simons, A plasticity concrete material model for DYNA3D, International Journal of Impact Engineering 19 (9-10) (1997) 847–873. doi:10.1016/S0734-743X(97)00023-7.

[28] L. Malvar, J. Crawford, K&C Concrete material model release III: Automated generation of material model input, Tech. Rep. TR-99-24.3, Karagonian & Case (2000).

[29] Livermore Software Technology Corporation, LS-DYNA User Manual: Volume II - Material Models (Version R10.0), California (2017).

[30] F.-K. Chang, K.-Y. Chang, A Progressive Damage Model for Laminated Composites Containing Stress Concentrations, Journal of Composite Materials 21 (9) (1987) 834–855. doi:10.1177/002199838702100904.

[31] Sika Ireland Limited, SikaDur-30, Product Datasheet v.02.01, Sika Ireland Limited, Dublin (May 2017).

[32] Y. Sha, H. Hao, Laboratory Tests and Numerical Simulations of CFRP Strengthened RC Pier Subjected to Barge Impact Load, International Journal of Structural Stability and Dynamics 15 (02) (2015) 1450037. doi:10.1142/S0219455414500370.

[33] A. A. Mutalib, H. Hao, Numerical Analysis of FRP-Composite-Strengthened RC Panels with Anchorages against Blast Loads, Journal of Performance of Constructed Facilities 25 (5) (2011) 360–372. doi:10.1061/(ASCE)CF.1943-5509.0000199.

[34] A. A. Mutalib, H. Hao, Numerical Analysis of FRP-Composite-Strengthened RC Panels with Anchorages against Blast Loads, Journal of Performance of Constructed Facilities 25 (5) (2011) 360–372. doi:10.1061/(ASCE)CF.1943-5509.0000199.

[35] International Federation for Structural Concrete, Fib Model Code for Concrete Structures 2010, Model code, Ernst & Sohn (2013).

[36] X. Lu, J. Teng, L. Ye, Bond–slip models for FRP sheets/plates bonded to concrete, Engineering Structures 27 (6) (2005) 920–937. doi:10.1016/j.engstruct.2005.01.014.

[37] J. Yao, J. G. Teng, L. Lam, Experimental Study on Intermediate Crack Debonding in FRP-Strengthened RC Flexural Members, Advances in Structural Engineering 8 (4) (2005) 365–396. doi:10.1260/136943305774353106.

[38] L. Ombres, Prediction of intermediate crack debonding failure in FRP-strengthened reinforced concrete beams, Composite Structures 92 (2) (2010) 322–329. doi:10.1016/j.compstruct.2009.08.003.

[39] S. Hong, Effect of Intermediate Crack Debonding on the Flexural Strength of CFRP-Strengthened RC Beams, Mechanics of Composite Materials 50 (4) (2014) 523–536. doi:10.1007/s11029-014-9439-6.

[40] O. Büyüköztürk, T.-Y. Yu, Understanding and Assessment of Debonding Failures in FRP-Concrete Systems, in: 7th International Congress on Advances in Civil Engineering, Istanbul, 2006, p. 22.

[41] V. V. Mozgalev, N. R. Prokopchuk, The Choice of Best-Fit Mathematical Models of the Behaviour of Rubber Compounds for Finite Element Analysis, International Polymer Science and Technology 41 (9) (2014) 19–22. doi:10.1177/0307174X1404100905.

[42] M. Pajak, The influence of the strain rate on the strength of concrete taking into account the experimental techniques, Architecture Civil Engineering Environment 4 (3) (2011) 77–86.

[43] H. Jia, L. Yu, G. Wu, Damage Assessment of Two-Way Bending RC Slabs Subjected to Blast Loadings, The Scientific World Journal 2014 (2014) 1–12. doi:10.1155/2014/718702.

[44] H. Kimura, M. Itabashi, K. Kawata, Mechanical characterization of unidirectional CFRP thin strip and CFRP cables under quasi-static and dynamic tension, Advanced Composite Materials 10 (2-3) (2001) 177–187. doi:10.1163/156855101753396654.

[45] Sika Ireland Limited, Sika CarboDur S, Product Datasheet v.05.01, Sika Ireland Limited, Dublin (Sep. 2017).

[46] P. D. Smith, J. G. Hetherington, Blast and Ballistic Loading of Structures, Butterworth-Heinemann, Oxford, 1994.

[47] A. Maazoun, B. Belkassem, B. Reymen, S. Matthys, J. Vantomme, D. Lecompte, Blast response of RC slabs with externally bonded reinforce-

570   ment: Experimental and analytical verification, Composite Structures 200 (2018) 246–257. `doi:10.1016/j.compstruct.2018.05.102`.
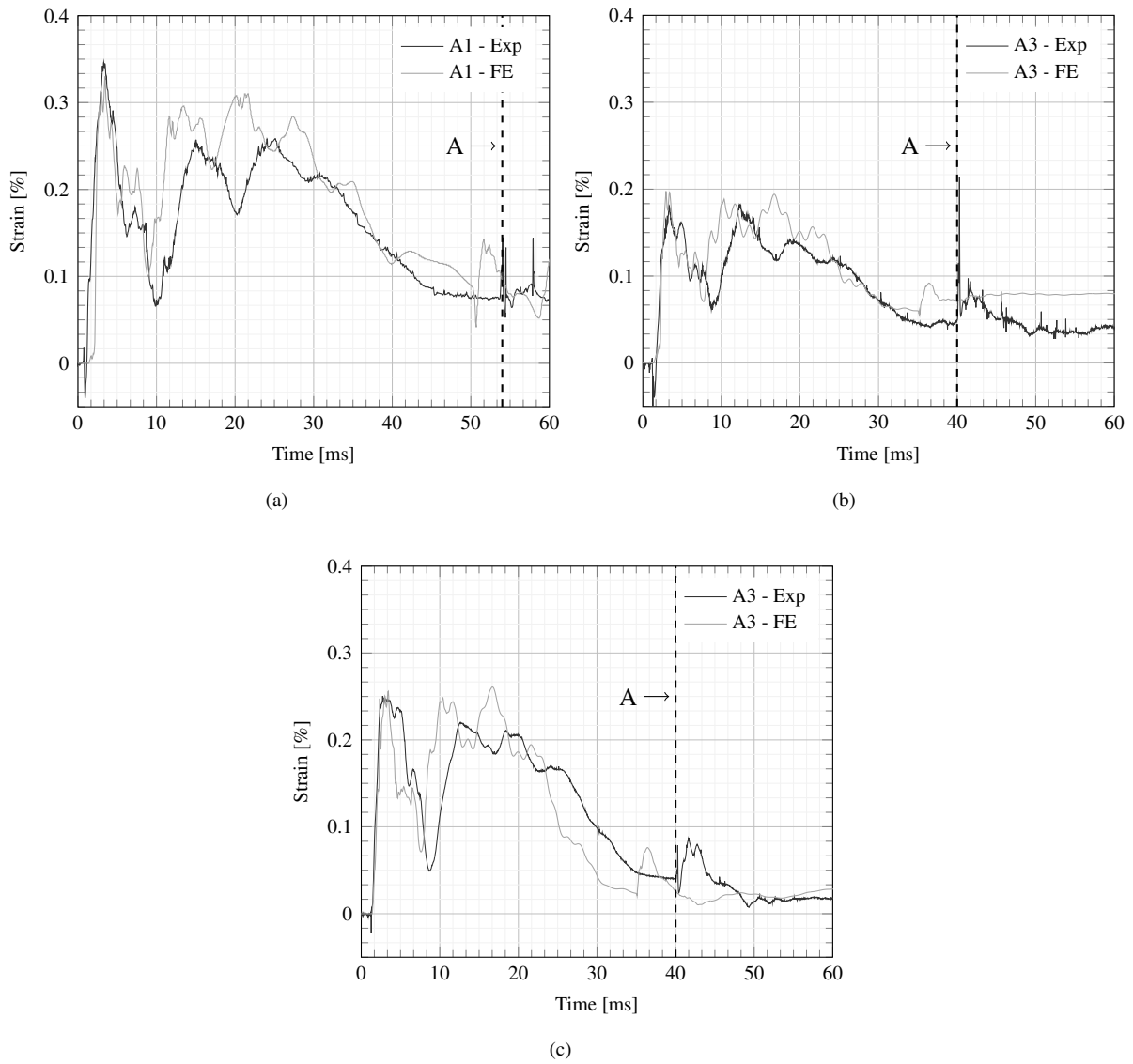
(a)

(b)

(c)

Figure 21: Comparison between experimental and numerical strain-time histories of the steel rebars for (a) specimen A1 and (b) specimen A3, and (c) strain-time history of the CFRP for specimen A3 (time label A indicates the experimental time at the impact between the slab and the EDST.
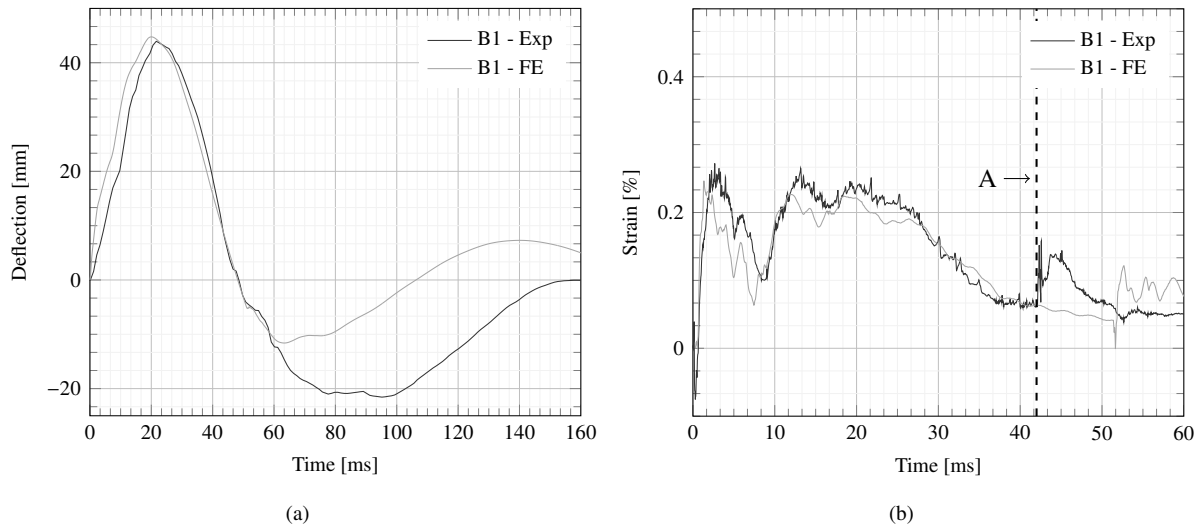
(a)

(b)

Figure 22: Comparison between experimental and numerical (a) deflection-time history and (b) strain in the reinforcing steel bars of specimen B1 (time label A indicates the experimental time at the impact between the slab and the EDST).
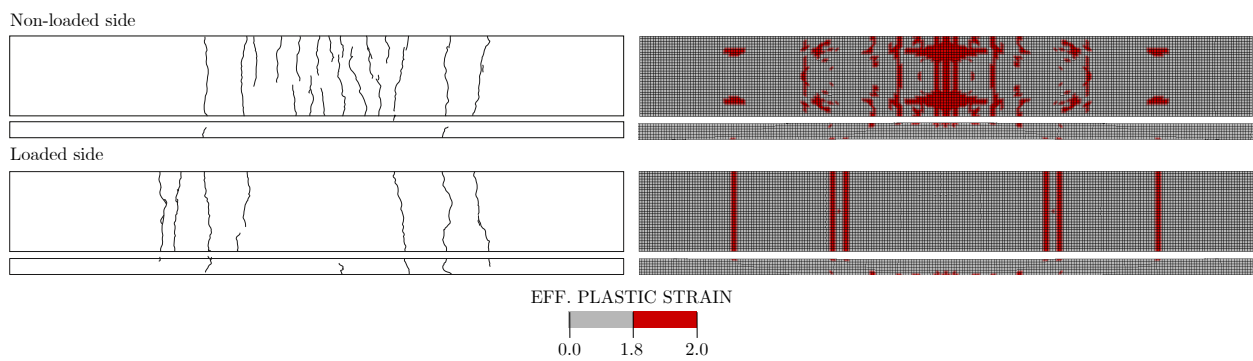

Figure 23: Experimental crack location and corresponding numerical predictions for specimen B1.

33